Research Square

Preprints are preliminary reports that have not undergone peer review.
They should not be considered conclusive, used to inform clinical practice,
or referenced by the media as validated information.

Extrusion-based 3D printing of 3YSZ–calcium phosphate composite scaffolds

C. C. Carmo
Universidade Nova de Lisboa
R. Barbosa
Universidade Nova de Lisboa
C. Bianchi
Universidade Nova de Lisboa
M. Brito
Universidade Nova de Lisboa
A. Rovisco
Universidade Nova de Lisboa
A. Baptista
Universidade Nova de Lisboa
J. Marques
University of Lisbon
I. Ferreira
imf@fct.unl.pt

Universidade Nova de Lisboa

Research Article

Keywords:

Posted Date: November 12th, 2026

DOI: https://doi.org/10.21203/rs.3.rs-11375679/v1

License: This work is licensed under a Creative Commons Attribution 4.0 International License.
Read Full License

Additional Declarations: No competing interests reported.

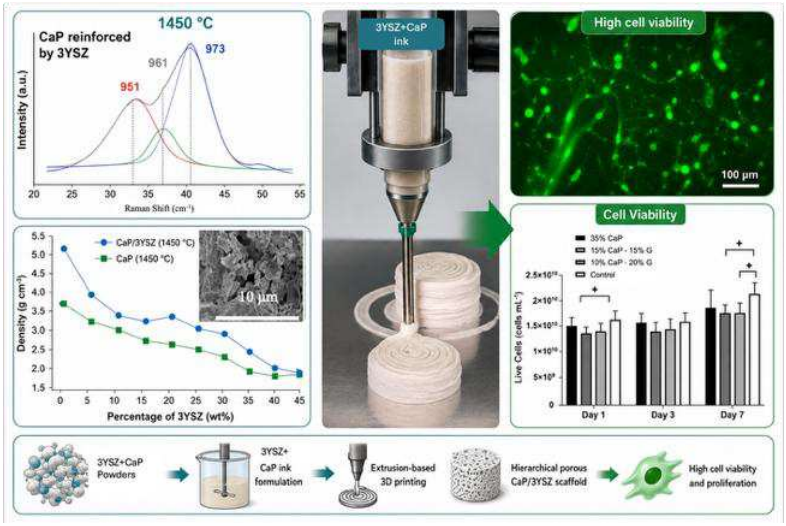
Extrusion-based 3D printing of 3YSZ–calcium phosphate composite scaffolds

C.C. Carmo[1], R. Barbosa[1], C. Bianchi[1], M. Brito[1], A. Rovisco[1], A. Baptista[1], J. Marques[2], I. Ferreira[1*].

[1]CENIMAT|i3N, Department of Materials Science, School of Science and Technology, NOVA University Lisbon, Caparica 2829-516, Portugal

[2]Oral Biology and Biochemistry Research Group, Faculdade de Medicina Dentária, UICOB, Universidade de Lisboa, Lisboa, Portugal

*imf@fct.unl.pt



Abstract

Extrusion-based 3D printing was employed to fabricate scaffolds from ceramic pastes comprising 3 mol% yttria-stabilised zirconia (3YSZ) and tricalcium phosphate ($Ca_3(PO_4)_2$, CaP). Pristine 3YSZ exhibited densities of 3.5–5.2 g cm^{-3}, substantially exceeding the density of natural bone. Incorporation of 30–45 wt% CaP reduced the density to 2.2–2.5 g cm^{-3}, approaching bone-like values. X-ray diffraction and Raman spectroscopy confirmed the stability of the tetragonal zirconia phase and the formation of phosphate-related phases attributed to hydroxyapatite (HAp) and β-tricalcium phosphate (β-TCP). The optimized composites combined reduced density with good phase stability and mechanical performance. Compact cylindrical specimens exhibited a Young's modulus of 524 ± 88 MPa and an ultimate

compressive strength of 180 ± 5.8 MPa. Notably, HGF-1 fibroblast viability and adhesion remained comparable to the control over seven days. These results demonstrate the potential of 3YSZ–CaP composites as lightweight, mechanically robust materials for bone-mimetic scaffolds.

Introduction

Bioceramic materials have been extensively studied for applications in dental implants, bone grafts, and tissue engineering scaffolds due to their chemical inertness, high hardness, and excellent wear resistance. Among these, alumina, zirconia, and hydroxyapatite (HAp) are the most widely investigated. Alumina and zirconia exhibit high density, superior mechanical strength, corrosion resistance, and biocompatibility, rendering them suitable for load-bearing applications such as hip and knee replacement [1]. Hydroxyapatite, a calcium phosphate bioceramic with a composition close to that of mammalian bone, is particularly valued for its osteogenic properties. However, its limited load-bearing capacity restricts its application primarily to coatings on metallic implants, such as titanium dental root implants and hip prostheses, where it enhances biocompatibility and reduces the risk of bone rejection [2].

Despite these advantages, the inherent brittleness of bioceramics remains a significant limitation, hindering their widespread, rapid and cost-effective adoption. Consequently, metallic implants continue to dominate the field of biomedical devices. The emergence of advanced manufacturing techniques, particularly additive manufacturing (3D printing), has created new opportunities for fabricating bioceramic structures. While conventional subtractive techniques remain prevalent, additive 3D printing has recently attracted attention as a promising approach to produce porous bioceramic matrices with enhanced design flexibility and controlled architectures [3,4,5,6].

To combine the mechanical strength of zirconia with the osteointegration capability of HAp, numerous studies have focused on zirconia-HAp composites. Co-precipitation methods have been employed to synthesise 3YSZ-HAp composites with varying compositions. In addition, scaffolds containing 20-30 wt% HAp combined with 3Y-ZrO_2 have been fabricated using digital light processing (DLP) involving powder mixing, photopolymerization, and subsequent sintering [7,8]. Other approaches include developing Y-ZrO_2 constructs coated with biopolymers to enhance the bioactivity of Y-ZrO_2 [9]. Zirconia-toughened HAp composites have shown particularly promising results; for example, doping HAp with 6 wt% ZrO_2

achieved a relative density of 90.7 % after sintering at 1200 ºC, significantly improving toughness and mechanical properties [10,11]. Similarly, microwave-assisted synthesis of zirconia-doped HAp ceramics has shown notable effects on shrinkage anisotropy, compressive strength, and microstructural characteristics [12].

The density of cortical bone typically ranges from 1 to 2 g cm^{-3} [13] while its mechanical properties lie between 160-250 MPa in compressive strength and 5-23 GPa in elastic modulus [14]. In contrast, conventional metallic implants such as titanium exhibit significantly higher densities (approximately 4.4 g cm^{-3}), with elastic modulus greater than 50 GPa, which may result in the incorporation of relatively heavy parts and modulus mismatch with bone can lead to bone loss around the implant over time. Therefore, magnesium alloys have attracted increasing interest as alternative materials due to their lower density (1.7-2 g cm^{-3}) and mechanical properties that are more closely approximating those of natural bone [14].

However, metallic materials generally have limited osteointegration and many present issues such as ion release, corrosion, and mechanical mismatch, which can lead to degradation at the implant-bone interface [15]. These limitations underline the importance of developing materials that more closely mimic the structure and composition of natural bone. Since 3YSZ is already established in medical and dental applications, reducing its density while retaining suitable mechanical performance could broaden its use in bone-replacement and scaffold applications. In this work, extrusion-based 3D printing of ceramic pastes was used to produce 3YSZ–CaP composite structures with controlled composition and sintering conditions. The aim was to reduce the density of printed 3YSZ components through incorporation of a calcium phosphate precursor, while maintaining the tetragonal zirconia phase and introducing bioactive phosphate phases. The resulting materials were evaluated in terms of density, phase composition, microstructure, compressive behaviour, and preliminary in vitro response using HGF-1 fibroblasts.

Experimental Details

Extrusion-based 3D printing of ceramic pastes was used to obtain cylindrical specimens (10 mm in diameter × 20 mm in height) and disc-shaped specimens (8 mm in diameter × 4 mm in height). The compositions consisted of 3 mol% yttria-stabilised zirconia (3YSZ), tricalcium phosphate ($Ca_3(PO_4)_2$); hereafter abbreviated as CaP), used as the calcium phosphate precursor, and, in selected formulations, graphite (G). The specimens were designed using CAD software

(Autodesk Meshmixer) with their dimensions pre-scaled to compensate for composition- and temperature-dependent shrinkage during sintering. Following extrusion using a Focus 3D printer, the printed specimens were dried at room temperature under ambient conditions and subsequently sintered at 1250, 1350 or 1450 ºC for 2 h in Nabertherm LHT 08/18 furnace. The ceramic pastes were prepared by mixing 3YSZ powder (TZ-3YS-E, Tosoh Corporation, Japan), with $Ca_3(PO_4)_2$ (Sigma-Aldrich, Germany) and/or graphite powder, (<20 μm, synthetic, Switzerland). The powder mixture was combined with a polymer binder and a surfactant based on the procedure described in Ref.[16]. The binder and surfactant contents were adjusted according to the powder composition to obtain an extrudable paste with a viscosity suitable for dispensing through a 21G needle using a 2 mL syringe. Rheological characterization revealed a continuous decrease in viscosity with increasing shear rate, indicating a shear-thinning behaviour. Power-law fitting yielded a flow behaviour index (n) of 0.203 and a consistency index (K) of 163.9 $Pa \cdot s^n$ (adjusted $R^2 = 0.9993$), confirming the pseudoplastic nature of the ceramic paste. This behaviour is advantageous for extrusion-based 3D printing, as it facilitates flow through the nozzle while ensuring adequate shape retention after deposition. As the rheological behaviour was governed primarily by the polymer binder and surfactant system, these values were considered representative of all paste formulations investigated. The overall production process, including CAD design, 3D printing, and specimens before and after sintering, is illustrated in Supplementary Information, Figure S1.

Elemental composition was analysed by energy-dispersive X-ray spectroscopy (EDS; Bruker Nano XFlash® MIN-SVE). Crystalline phases were identified using X-ray diffraction (XRD; XRDynamic 500, Anton Paar) over a 2θ range of 10°–90°, using a step size of 0.011°, and a counting time of approximately 30 s per step. Surface morphology was examined by scanning electron microscopy (SEM; Hitachi SU8220) at an accelerating voltage of 5 kV after sputter-coating samples with an approximately 20 nm Au-Pd (80:20) layer using a Quorum Q150T ES sputter coater. Raman spectroscopy (Witec Alpha 300 RAS) with a 532 nm laser operating at 0.6 mW was used to provide complementary compositional and structural information. In addition, the specimens were examined using an optical microscope (Leica DMi8) equipped with a fluorescent filter to compare their surface appearance before and after the cell viability assays.

Compressive strength was determined using cylindrical specimens tested on a universal testing machine (Autograph Shimadzu AG-50kNG) at a crosshead speed of 1 mm min^{-1}.

To biological response of soft tissue cells was evaluated using human gingival fibroblasts (HGF-1; ABM®, Canada). Cell cultured was performed aseptically in a laminar-flow cabinet (Biobase®, China). Cryopreserved cells were thawed and expanded in 75 cm^3 tissue culture flasks containing Dulbecco's modified Eagle's medium (DMEM; Lonza®, Switzerland), supplemented with 10% foetal bovine serum (Biowest®, France) and 1% penicillin-streptomycin solution (Applied Biological Materials Inc., Canada). Cultures were maintained at 37 °C, in a humified atmosphere containing 5% CO_2 and 98 % relative humidity using a cell culture incubator (Memmert®, Schwabach, Germany). The culture medium was replaced after the first 24 h and subsequently every two days until the cells reached the required confluence.

Upon reaching approximately 80% confluence (after approximately 7 days), the cells were detached using Trypsin-EDTA solution (Lonza™, Switzerland) for 5-10 min, stained with Trypan Blue (AMRESCO®, USA), and counted using a Neubauer haemocytometer (Laboroptik Ltd., UK) under an inverted phase-contrast microscopy (Olympus CK2). The cell suspension was adjusted to seeding density of 1×10^4 cells in 500 µL of culture medium per well in sterile 48-well tissue culture plates.

Prior to cell seeding, the disk-shaped specimens were identified and sterilised by two consecutive ultrasonic baths in 70% ethanol for 30 min each, followed by a final rinse with 70% ethanol and ultraviolet irradiation for an additional 30 min. The sterilised specimens were transferred to sterile 48-well plates (Corning Inc®, USA) and pre-incubated with complete culture medium for 1 h to promote protein adsorption before cells seeding. HGF-1 cells were then seeded onto each specimen at the prescribed density. Control wells containing cells culture directly on the tissue culture plate in complete medium were included for each experimental group.

Cell viability and proliferation were assessed after 1, 3, and 7 days using the CellTiter-Blue® reagent (Promega®, USA). Fluorescence intensity, corresponding to the mitochondrial reduction of resazurin, was measured at excitation and emission wavelengths of 530/30 nm and 595/10 nm, respectively, using a VICTOR Nivo™ HH3500 microplate reader (PerkinElmer®, UK). For SEM observation of cell morphology, the specimens were fixed in 1.5% glutaraldehyde and dehydrated through a graded ethanol series prior to imaging.

Statistical analyses were performed using GraphPad Prism 11 for Windows (GraphPad Software, Inc., San Diego, CA, USA). As the experimental design included two independent

variables (incubation time and material composition), the data were analysed by two-way analysis of variance (ANOVA) to evaluate the main effects of each facto and their interaction. When significant differences were detected, Tukey's multiple comparisons test was applied for post hoc analysis. Statistical significance was established at $p < 0.05$.

Results and Discussion

CaP and 3YSZ powders were mixed in varying weights fractions, and the resulting density changes as shown in Figure 1 and Table 1. Increasing the CaP content relative to 3YSZ systematically reduces the density of the 3DP samples for both 1250 and 1450 ºC sintering temperatures (Figure 1). However, it was experimentally observed that when the CaP content exceeded 50 wt%, the samples become extremely fragile, breaking upon handling or releasing significant amounts of material when immersed in simulated body fluid (SBF), rendering them unsuitable for implant application.

To obtain density below 3 g cm^{-3}, compositions with up to 45 wt% CaP and sintering temperature of 1250 ºC were selected. Additional compositions were also explored, including the incorporation of graphite, either as a partial replacement for CaP or in combination with it, as shown in Table 1.

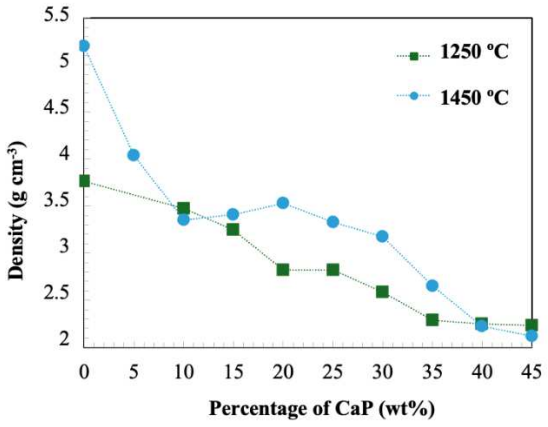


Figure 1 – Influence of CaP percentage on the density of sintered samples constituted by 3YSZ and CaP sintered at 1250ºC and 1450ºC.

Table 1 – Density of different 3YSZ composites and sintering temperatures tested.

Composition (wt%)			Density (g cm^{-3})	
YSZ	G	CaP	1250 ºC	1450 ºC
100	0	0	3.8	5.2
95	5	0	2.8	3.8
90	10	0	3.8	3.7
85	15	0	2.9	3.3
80	20	0	3.8	3.3
70	20	10	2.0	2.5
70	15	15	2.2	2.6
50	20	30	1.6	1.5
85	10	5	3.7	3.3

The structural modifications induced by CaP incorporation were analysed by X-ray diffraction (XRD). Phase identification was made based on reference patterns and literature data [17],[18],[19],[20],[21],[22], and all diffractograms were indexed accordingly. Figure 2a compares samples containing 0, 5, 15, 35 and 45 wt% CaP sintered at 1250 °C, while Figure 2b shows the influence of sintering temperature (1250, 1350 and 1450 °C) for samples with 35 wt% CaP. All samples exhibit the characteristic diffraction peaks of tetragonal zirconia (t-ZrO_2) at approximately 30°, 35°, 50° and 60° (2θ), confirming the stability of the tetragonal phase of 3YSZ across all compositions. At low CaP contents (5–15 wt%), sharp and well-defined t-ZrO_2 peaks are observed, with no detectable secondary phases, indicating that samples are predominantly composed of tetragonal YSZ, even at sintering temperature of 1250ºC. In contrast, higher CaP contents (35–45 wt%) promote the appearance of additional peaks associated with calcium phosphate phases, namely β-tricalcium phosphate (β-TCP) and hydroxyapatite (HAp). Weak contributions from monoclinic zirconia (m-ZrO_2) may also be present, however, these overlap with phosphate-related peaks, making identification ambiguous.

The influence of sintering temperature (1250 -1450 °C) on samples containing 35 wt% CaP is shown in Figure 2b. The diffractograms reveal an increase in peak intensity with increasing temperature, indicating enhanced crystallinity and the development of more pronounced HA/β-TCP phases. The peak positions remain unchanged, consistent with thermal stability of the tetragonal phase.

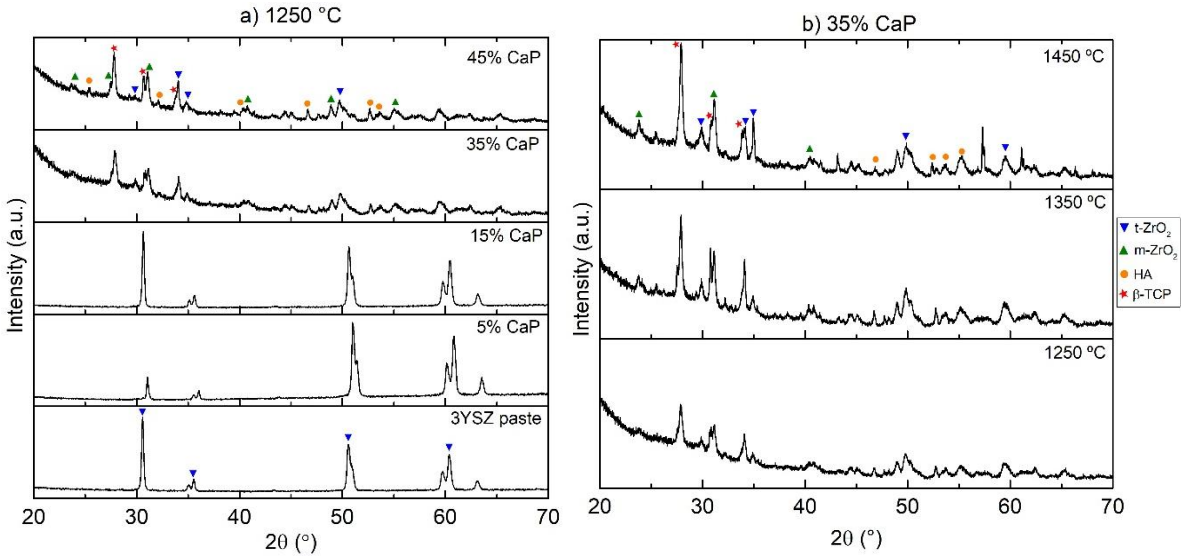


Figure 2 – XRD patterns of 3YSZ–CaP composites containing: a) 5, 15, 35, and 45 wt% CaP, and pure 3YSZ, sintered at 1250 °C; and b) 35 wt% CaP, sintered at 1250, 1350, and 1450 °C. Diffraction peaks corresponding to t-ZrO_2, m-ZrO_2, HAp and β-TCP as identified in legend.

To reduce the density of samples produced with lower CaP % (10-25%) the incorporation of graphite was also investigated. This approach was expected to enhance mechanical properties, particularly toughness, as reported by other authors [23], due to the ability of graphite to hinder crack propagation by acting as a crack-bridging phase. For graphite-containing samples with low CaP content (e.g.,10 wt% CaP–20 wt% G and 15 wt% CaP–15 wt% G at 1250 °C), the XRD patterns show a dominant t-ZrO_2 phase, with only minor contributions from monoclinic zirconia (m-ZrO_2) and/or HAp and β-TCP phases. In comparison with samples containing 35 wt% CaP (with a similar total content relative to YSZ), it is evident that CaP plays the primary role in driving structural modifications. However, when comparing samples containing 15 wt% CaP alone with those containing 15 wt% CaP plus graphite (G), the appearance of β-TCP peaks is observed only in the graphite-containing samples, suggesting that graphite incorporation may influence phase evolution. The XRD patterns of these compositions resemble those obtained for samples with higher CaP content (e.g., 35 wt% CaP, as shown in Figure 3), indicating a tendency towards increased phase complexity. In contrast, compositions with higher CaP content processed at elevated temperature (e.g., ~30 wt% CaP at 1450 °C) exhibit a clearly multiphase structure, with coexisting t- and m-ZrO_2 phases alongside well-defined HAp and β-TCP peaks.

Overall, increasing CaP content and sintering temperatures promotes the coexistence of m-ZrO_2 with β-TCP and HAp phases, indicating enhanced phase segregation and crystallization of calcium phosphate phases.

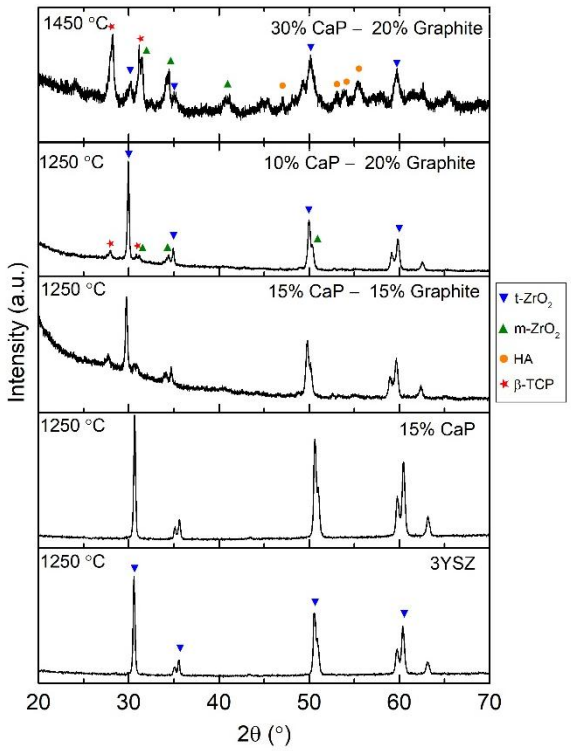


Figure 3 – XRD patterns of 3YSZ–CaP–Graphite composites sintered at 1250 °C and 1450 °C. The series includes CaP–Graphite compositions of 10–20, 15–15, and 30–20 wt%, together with 15 wt% CaP and pure 3YSZ references. Diffraction peaks corresponding to t-ZrO_2, m-ZrO_2, HA, and β-TCP are identified.

To complement the XRD results, Raman spectroscopy was performed to probe the local structure and confirm phase stability. Figure 4 shows the Raman spectra of 3YSZ–CaP composites containing 0, 10, 25, and 45 wt% CaP (and pure 3YSZ), sintered at 1250 °C and 1450 °C. Red dashed lines indicate the characteristic tetragonal zirconia (t-ZrO_2) modes at ~150, 265, 320, 475 and 640 cm^{-1}, corresponding to the E_g, B_{1g} and A_{1g} vibrations of the $P4_2/nmc$ structure [24]. All samples exhibit these bands, confirming retention of the t-ZrO_2 phase after both sintering treatments. In the compositions 25 and 45 wt% CaP, weak additional peaks at ~102, 179, 305, 332 and 378 cm^{-1} indicate traces of monoclinic zirconia (m-ZrO_2) phase [24].

The Raman spectra of β-TCP and HAp share internal vibrational modes associated with PO_4^{3-} groups. In HAp, the most intense feature corresponds to the symmetric stretching (ν_1) P–O

mode at 962 cm^{-1}, typically observed as a single strong peak, accompanied by lower-intensity bands in the 1020-1095 cm^{-1} range attributed to asymmetric stretching modes (ν_3). Additional bands arise from O–P–O doubly degenerate bending modes (ν_2) at 400–490 cm^{-1} and triply degenerate modes (ν_4) at 570–625 cm^{-1}. For β-TCP, the principal vibrations likewise originate from the symmetric stretching (ν_1) P–O mode, appearing as a doublet at 948 and 970 cm^{-1}, together with lower-intensity bands at 995–1120 cm^{-1} due to asymmetric stretching modes (ν_3). The O–P–O bending modes (ν_2) occur at 370–505 cm^{-1}, while the triply degenerate modes (ν_4) are observed at 530–645 cm^{-1} [25–27]. Some t-ZrO_2 modes may overlap with lower-intensity phosphate-related bands; however, they do not coincide with the most intense phosphate peaks in the 900–1200 cm^{-1} region. For the composition 10 wt% CaP, the band at 971 cm^{-1} is barely detectable, indicating that the phosphate phase is finely dispersed within the zirconia matrix [26]. As the CaP content increases, these bands become progressively sharper and more intense, suggesting enhanced CaP crystallisation and partial segregation from the zirconia phase [24]. The deconvolution of PO_4^{3-} bands in the 900-1000 cm^{-1} region in three peaks led to obtain a low intensity peak at 945 cm^{-1} a second peak at 954 cm^{-1} and the most intense peak at 971 cm^{-1}. They are clearly attributed to β-TCP, but the presence of a peak close to HAp might be correlated with HAp formation, as also observed by XRD data (Figure S3). SEM images of the sample containing 45 wt% CaP reveal clearly distinct regions: granular areas corresponding to 3YSZ and smoother regions associated with the CaP phase, which appears to be dispersed throughout the materials and exhibits a morphology suggestive of low temperature melting region. Energy-dispersive spectroscopy (EDS) confirms the presence of C, Zr, Ca, P and O (Figure S2 supplementary information). Although the overall morphology remains similar across samples, the extent of these smoother regions increases with increasing CaP content.

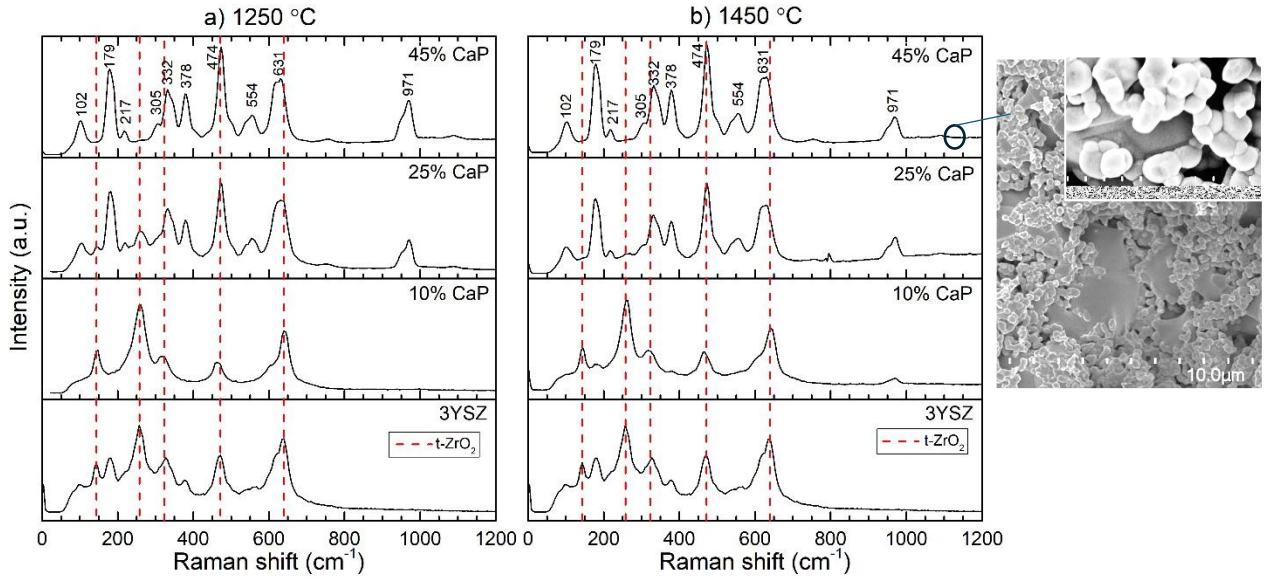


Figure 4 – Raman spectra of the 3YSZ–CaP composites, for CaP contents of 45, 25, 10 wt%, sintered at a) 1250 °C and b) 1450 °C, and pure 3YSZ. Red dashed lines mark the characteristic Raman modes of t-ZrO_2. SEM images of 45% CaP samples with scale of 10µm and 1µm.

To assess the effect of graphite addition used as a pyrogen, Raman spectra of 3YSZ–CaP–Gr composites sintered at 1250 °C were analysed (Figure 5). The characteristic D band at ~1350 cm^{-1} (A_{1g} breathing mode of sp^2 carbon) and G band at ~1580 cm^{-1} (E_{2g} bond-stretching of sp^2 sites) are absent in all composite spectra, confirming complete removal of graphite during sintering [28]. The t-ZrO_2 modes remain clearly visible at ~150, 265 and 320 cm^{-1} (E_g and B_{1g} vibrations) and at ~475 and ~640 cm^{-1} (A_{1g} vibrations), indicating that carbon did not induce deleterious phase transformations [24,27]. The CaP-related phosphate bands also persist, demonstrating the retention of the phosphate phase [26]. Minor variations in band intensity between the graphite-containing and graphite-free samples suggest that porosity development affects Raman scattering efficiency and local crystallinity of the ceramic matrix.

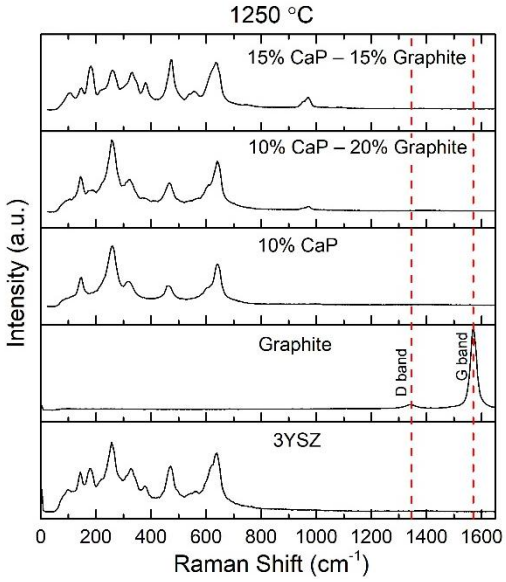


Figure 5 – Raman spectra of 3YSZ–CaP–Graphite composites with CaP–Graphite contents of 15–15 and 10–20 wt%, along with 10 wt% CaP, sintered at 1250 °C, pure graphite and pure 3YSZ. Red dashed lines mark the characteristic D and G bands of graphite.

HGF-1 fibroblast viability was composition-dependent (Figure 6). The 35 wt% CaP group showed the most stable cellular response over the 7-day culture period. Two-way analysis of variance (ANOVA) demonstrated that both incubation time and material composition had a statistically significant effect on fluorescence intensity ($p < 0.05$). The number of specimens analysed was progressively reduced during the experimental period (n=10 on day 1, n=8 on day 3, and n=6 on day 7) owing to the removal of sample for SEM observation of cell morphology (Supplementary Information, Figure S4).

On day 1, the 35 wt% CaP group showed significantly higher cell viability than the 15 wt% CaP- 15 wt% G group, whereas no statistically significant difference was observed between 35 wt% CaP group and the control. By day 3, no significant differences in cell viability were detected among the experimental groups. On day 7, the graphite-containing compositions exhibited significantly lower cell viability than the control group. These results of Figure 6 suggest favourable preliminary cytocompatibility for the 35 wt% CaP composition, although further studies using osteogenic cell models are required to assess bone-regenerative potential.

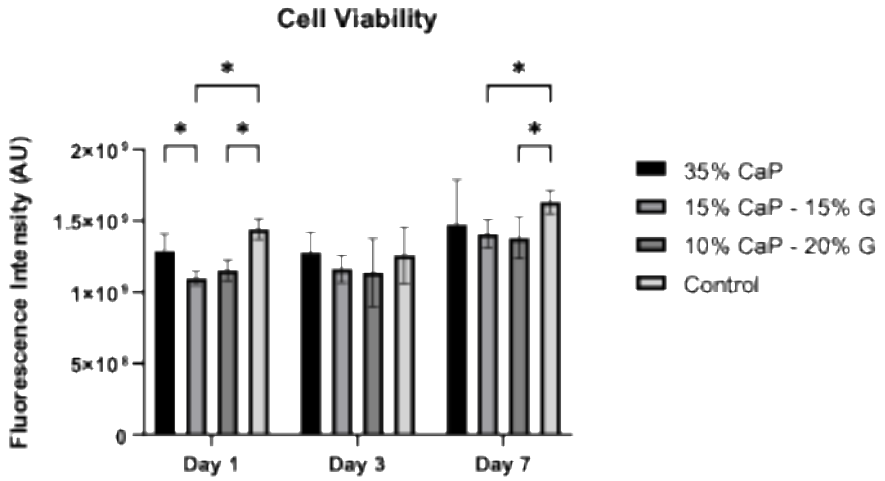


Figure 6 - HGF-1 Cell Viability. Results are expressed as arbitrary units (AU) of fluorescence intensity. Data are presented as mean ± standard deviation for 35 wt% CaP, 15 wt% CaP – 15 wt% G, and 10 wt% CaP – 20 wt% G (all sintered at 1250ºC), alongside a control (cells seeded on polystyrene). Measurements were taken at 1, 3, and 7 days of culture. Initial sample size was n=10 (day 1), followed by n=8 (day 3) and n=6 (day 7) due to sample removal for SEM analysis. Asterisks denote statistical significance between groups (*$p < 0.05$, Two-way ANOVA, Tukey's test).

Discussion

The main objective of this work was to reduce the density of extrusion-printed 3YSZ ceramics while retaining mechanically relevant strength and stiffness, through the incorporation of calcium phosphate (CaP) phases with potential bioactivity. Fully dense sintered 3YSZ typically exhibits a density exceeding 6 g cm^{-3} [29]. In contrast, the extrusion-printed 3YSZ specimens investigated in this work exhibit lower densities owing to the intrinsic porosity associated with paste-based printing and incomplete densification during sintering. Depending on the sintering temperature, the density of the printed 3YSZ samples ranged from 3.5–3.8 g cm^{-3} at 1250ºC to 5.2 g cm^{-3} at 1450ºC. Although these values are lower than those of fully dense 3YSZ, the resulting densities remain high for bone-replacement applications, particularly for large components. Therefore, calcium phosphate incorporation was investigated as a strategy to further reduce density while enhancing bioactivity through the introduction of phosphate phases.

Zirconia-calcium phosphate composites are particularly attractive for biomedical applications because they combine the mechanical reliability of tetragonal zirconia (t-ZrO_2) with potential

bioactivity of hydroxyapatite (HAp) and β-tricalcium phosphate (β-TCP). Their composition must therefore be carefully optimised to preserve the mechanical contribution and phase stability of zirconia while incorporating a controlled fraction of calcium phosphate phases. This balance suggests that intermediate CaP contents and relatively low sintering temperatures may be advantageous for biomedical applications [30]. In the present study, the lowest density was obtained for the composition containing 50 wt% 3YSZ, 20 wt% C, and 30 wt% CaP; however, these samples were also mechanically fragile. A more favourable compromise between density reduction and mechanical results was achieved with CaP contents of 30–45 wt%, at a sintered temperature of 1250 ºC, resulting in densities of 2.2–2.5 g cm^{-3}.

Structural characterisation of the samples sintered at 1250 °C and 1450 °C revealed predominantly t-ZrO_2-related vibration bands, which remain essentially unchanged across the different compositions, indicating that the tetragonal zirconia phase was largely preserved under the investigated process conditions [24]. As the CaP content increase, a band centred at 971 cm^{-1} become increasingly discernible, reaching its highest intensity in the samples containing 45 wt% CaP and sintered at 1250 °C. HAp phase was clearly detected in the samples sintered at 1450 ºC. These findings indicate that increasing the sintering temperature promotes the development of crystalline phosphate phases and modifies the intensity of the corresponding vibrational bands without substantially altering the zirconia-related spectral features. SEM analysis further revealed zirconia grains embedded in more continuous CaP-rich matrix. This microstructural arrangement may contribute to a more compliant mechanical response, although it can reduce hardness.

The most favourable combination of reduced density and mechanical performance was obtained for the composition containing 35 wt% CaP. Compact cylindrical specimens (Figure S1) exhibit a Young's modulus of 524 ± 88 MPa and an ultimate compressive strength of 180 ± 5.8 MPa. The compressive strength falls within the range reported for cortical bone, whereas the lower Young's modulus indicates a more compliant response. Hollow cylindrical samples with an external diameter of 10 mm, internal diameter of 5 mm and height 20 mm, exhibited a Young's modulus of 545 ± 262 MPa and a lower ultimate compressive strength of 16.3 ± 5 MPa. The lower compressive strength of the hollow samples is consistent with their reduced load-bearing cross-sectional area and the increase susceptibility of their geometry to local stress concentrations, buckling and crack initiation and propagation.

The mechanical performance of the present materials can be contextualised by comparison with previously reported calcium phosphate-based and zirconia-containing ceramic systems. For

example, digital light processing (DLP) of wollastonite fibres has enabled the fabrication of calcium phosphate-based ceramic scaffolds with a whitlockite matrix, and a compressive strength of 31.0 MPa, representing a promising performance level for porous bone scaffolds produced using desktop DLP systems [31]. Similarly, composites containing alumina, zirconia and hydroxyapatite powders, sintered at 1600 °C, exhibited compressive strengths of up to 68.17 MPa for compositions containing 15 wt% HAp [32]. In another study, bulk sintered composites comprising 70 wt% β-TCP and 30 wt% HAp were reinforced with different amounts of 3YSZ and sintered at 1200 °C to develop toughened bone-substitute materials. A maximum compressive strength of 150 MPa was reported for specimens containing 3 vol% 3YSZ [33]. Furthermore, the combination of 3D printing with Zn-doped hydroxyapatite/glass composites has enabled the fabrication of complex scaffolds with compressive strengths of approximately 90 MPa [34]. Zirconia–hydroxyapatite composites prepared from powder mixtures without prior compaction and subsequently sintered have also demonstrated compressive strengths of approximately 172 MPa for compositions containing 20 wt% HAp and 87 MPa for those with 40 wt% HAp [35].

Although, some previously reported systems exhibit higher compressive strengths than the hollow samples developed in this study, direct comparisons must account for differences in composition, porosity, specimen geometry, fabrication methos and mechanical testings conditions. Notably, the compact specimens containing 35 wt% CaP achieved a compressive strength of 180 ± 5.8 MPa, comparing favourably with several previously reported zirconia-calcium phosphate composites. Overall, these results demonstrate the potential of the proposed extrusion-printing approach to produce lightweight ceramic components with a competitive balance between density reduction and mechanical performance. This combination is particularly relevant to the development of bone-mimetic materials and load-bearing scaffolds, for which both mechanical integrity and reduced density are important considerations. Furthermore, preliminary cytocompatibility results for the composition containing 35 wt% CaP were favourable, supporting further investigation of its biomedical potential. Additional studies using osteogenic cell models are required to evaluate osteogenic differentiation, bone-forming capacity and the potential of these materials to support bone regeneration.

Conclusions

This study demonstrates the feasibility of tailoring the density, mechanical properties, and biological performance of 3YSZ-based ceramics through controlled incorporation of calcium phosphate and graphite using extrusion-based 3D printing. The addition of CaP was identified as the primary factor governing density reduction and the formation bioactive calcium phosphate phases, while preserving the stability of the tetragonal zirconia phase.

An optimal balance between density reduction and mechanical performance was achieved for compositions containing 30–45 wt% CaP, particularly following sintering at 1250 °C. Among these, the composition containing 35 wt% CaP exhibited the most favourable combination of properties, including a density comparable to that of cortical bone, competitive mechanical strength, and HGF-1 fibroblast adhesion and proliferation comparable to the control. Structural characterisation confirmed the formation of a multiphase composite comprising mechanically robust tetragonal zirconia and bioactive calcium phosphate phases, representing a favourable combination for load-bearing biomedical applications.

Overall, the findings demonstrated the potential of additively manufactured 3YSZ–CaP composites as bone-mimetic biomaterials, providing a promising strategy for the fabrication of lightweight, load-bearing scaffolds with enhanced biological functionality. Future work should focus on optimising pore architecture and evaluating long-term performance, including osteogenic cell lines and *in vivo* models to further assess their suitability for bone-regenerative applications.

Acknowledgments

This work was mainly funded by ERC-CoG-2014, CapTherPV, 647596, and partially funded by National Funds through the FCT – Fundação para a Ciência e a Tecnologia, I.P., Projects UID/50025/2025, LA/0037/2020, of the Associate Laboratory Institute of Nanostructures, Nanomodelling and Nanofabrication – i3N and PhD grant reference 2024.00651.BD and DOI identifier https://doi.org/10.54499/2024.00651.BD of C. C. Carmo.

Author contributions

C.C Carmo, R. Barbosa conducted the experiments and wrote the original draft of the manuscript, C. Bianchi and M-Brito developed the inks. A. Rovisco, A. Baptista, contributed

to data analysis and manuscript editing. J. Marques contributed with the biological tests and data analysis, I. Ferreira conceived the study and supervised the work. All authors reviewed and commented on the manuscript.

Declarations

Conflict of interest

The authors have no competing interests to declare.

Data availability

The data that support the resuts presented on this study are available from the corresponding author upon reasonable request.

Use of generative AI tools

No generative AI tools were used in the preparation of this work.

References

[1] C.Y. Hu, T.-R. Yoon, Recent updates for biomaterials used in total hip arthroplasty, Biomater Res 22 (2018) 33. https://doi.org/10.1186/s40824-018-0144-8.

[2] M. Ly, S. Spinelli, S. Hays, D. Zhu, 3D Printing of Ceramic Biomaterials, Engineered Regeneration 3 (2022) 41–52. https://doi.org/10.1016/j.engreg.2022.01.006.

[3] R. Galante, C.G. Figueiredo-Pina, A.P. Serro, Additive manufacturing of ceramics for dental applications: A review, Dental Materials 35 (2019) 825–846. https://doi.org/10.1016/j.dental.2019.02.026.

[4] G. Zhong, M. Vaezi, P. Liu, L. Pan, S. Yang, Characterization approach on the extrusion process of bioceramics for the 3D printing of bone tissue engineering scaffolds, Ceramics International 43 (2017) 13860–13868. https://doi.org/10.1016/j.ceramint.2017.07.109.

[5] Y. Wen, S. Xun, M. Haoye, S. Baichuan, C. Peng, L. Xuejian, Z. Kaihong, Y. Xuan, P. Jiang, L. Shibi, 3D printed porous ceramic scaffolds for bone tissue engineering: a review, Biomater. Sci. 5 (2017) 1690–1698. https://doi.org/10.1039/C7BM00315C.

[6] M. Vaezi, H. Seitz, S. Yang, A review on 3D micro-additive manufacturing technologies, Int J Adv Manuf Technol 67 (2013) 1721–1754. https://doi.org/10.1007/s00170-012-4605-2.

[7] J. Brzezińska-Miecznik, K. Haberko, M. Bucko, G. Grabowski, M. Sitarz, Hydroxyapatite of natural origin - zirconia composites, preparation and reactions within the system, PAC 10 (2016) 219–225. https://doi.org/10.2298/PAC1604219B.

[8] Y. Cao, T. Shi, C. Jiao, H. Liang, R. Chen, Z. Tian, A. Zou, Y. Yang, Z. Wei, C. Wang, L. Shen, Fabrication and properties of zirconia/hydroxyapatite composite scaffold based on digital light processing, Ceramics International 46 (2020) 2300–2308. https://doi.org/10.1016/j.ceramint.2019.09.219.

[9] K. Sakthiabirami, J.-H. Kang, J.-G. Jang, V. Soundharrajan, H.-P. Lim, K.-D. Yun, C. Park, B.-N. Lee, Y.P. Yang, S.-W. Park, Hybrid porous zirconia scaffolds fabricated using additive manufacturing for bone tissue engineering applications, Materials Science and Engineering: C 123 (2021) 111950. https://doi.org/10.1016/j.msec.2021.111950.

[10] S. Tarafder, V.K. Balla, N.M. Davies, A. Bandyopadhyay, S. Bose, Microwave-sintered 3D printed tricalcium phosphate scaffolds for bone tissue engineering: 3D Printed TCP Scaffolds for Bone Tissue Engineering, J Tissue Eng Regen Med 7 (2013) 631–641. https://doi.org/10.1002/term.555.

[11] J. Zhang, D. Huang, S. Liu, X. Dong, Y. Li, H. Zhang, Z. Yang, Q. Su, W. Huang, W. Zheng, W. Zhou, Zirconia toughened hydroxyapatite biocomposite formed by a DLP 3D printing process for potential bone tissue engineering, Materials Science and Engineering: C 105 (2019) 110054. https://doi.org/10.1016/j.msec.2019.110054.

[12] H. Fan, L. Wang, R. Dou, Properties of zirconia-doped hydroxyapatite ceramics prepared by vat photopolymerization additive manufacturing technology and microwave sintering, Ceramics International 51 (2025) 25662–25672. https://doi.org/10.1016/j.ceramint.2025.03.248.

[13] H.E. Meema, S. Meema, Compact Bone Mineral Density of the Normal Human Radius, Acta Radiologica: Oncology, Radiation, Physics, Biology 17 (1978) 342–352. https://doi.org/10.3109/02841867809127938.

[14] Poinern, G.E.J.; Brundavanam, R.K.; Fawcett, D., Nanometre scale hydroxyapatite ceramics for bone tissue engineering, (n.d.). https://doi.org/10.5923/j.ajbe.20130306.04.

[15] X. Lu, Y. Zhao, X. Peng, C. Lu, Z. Wu, H. Xu, Y. Qin, Y. Xu, Q. Wang, Y. Hao, D. Geng, Comprehensive Overview of Interface Strategies in Implant Osseointegration, Adv Funct Materials 35 (2025) 2418849. https://doi.org/10.1002/adfm.202418849.

[16] K. Sakthiabirami, J.-H. Kang, J.-G. Jang, V. Soundharrajan, H.-P. Lim, K.-D. Yun, C. Park, B.-N. Lee, Y.P. Yang, S.-W. Park, Hybrid porous zirconia scaffolds fabricated using

additive manufacturing for bone tissue engineering applications, Materials Science and Engineering: C 123 (2021) 111950. https://doi.org/10.1016/j.msec.2021.111950.

[17] A. Kumar, P. Kumar, A.S. Dhaliwal, Structural studies of zirconia and yttria doped zirconia for analysing it phase stabilization criteria, IOP Conf. Ser.: Mater. Sci. Eng. 1033 (2021) 012052. https://doi.org/10.1088/1757-899X/1033/1/012052.

[18] D. Xidaki, P. Agrafioti, D. Diomatari, A. Kaminari, E. Tsalavoutas-Psarras, P. Alexiou, V. Psycharis, E. Tsilibary, S. Silvestros, M. Sagnou, Synthesis of Hydroxyapatite, β-Tricalcium Phosphate and Biphasic Calcium Phosphate Particles to Act as Local Delivery Carriers of Curcumin: Loading, Release and In Vitro Studies, Materials 11 (2018) 595. https://doi.org/10.3390/ma11040595.

[19] O. Gorban, I. Danilenko, I. Nosolev, E. Abdullayev, A. Islamov, K. Gavrilenko, A. Doroshkevich, O. Shvets, S. Kolotilov, Impact of chemical and physical modification of zirconia on structure, surface state, and catalytic activity in oxidation of α-tetralol, J Nanopart Res 24 (2022) 197. https://doi.org/10.1007/s11051-022-05566-5.

[20] F. Bakan, A Systematic Study of the Effect of pH on the Initialization of Ca-deficient Hydroxyapatite to β-TCP Nanoparticles, Materials 12 (2019) 354. https://doi.org/10.3390/ma12030354.

[21] V.P. Padmanabhan, R. Kulandaivelu, D. Santhana Panneer, S. Vivekananthan, S. Sagadevan, J. Anita Lett, Microwave synthesis of hydroxyapatite encumbered with ascorbic acid intended for drug leaching studies, Materials Research Innovations 24 (2020) 171–178. https://doi.org/10.1080/14328917.2019.1624940.

[22] S. Ding, J. Zhao, Q. Yu, Effect of Zirconia Polymorph on Vapor-Phase Ketonization of Propionic Acid, Catalysts 9 (2019) 768. https://doi.org/10.3390/catal9090768.

[23] Q. Li, L. Shi, Y. Cai, X. Wang, L. Li, Z. Yuan, W. Tang, Z. Zhan, Effect of graphite on microstructure and friction-wear properties of yttria-stabilized zirconia coatings, Ceramics International 50 (2024) 54116–54124. https://doi.org/10.1016/j.ceramint.2024.10.268.

[24] P.N. Kumar, S. Kannan, Quantitative analysis of the structural stability and degradation ability of hydroxyapatite and zirconia composites synthesized in situ, RSC Adv. 4 (2014) 29946. https://doi.org/10.1039/C4RA02441A.

[25] R. Cuscó, F. Guitián, S. de Aza, L. Artús, Differentiation between hydroxyapatite and β-tricalcium phosphate by means of μ-Raman spectroscopy, Journal of the European Ceramic Society 18 (1998) 1301–1305. https://doi.org/10.1016/S0955-2219(98)00057-0.

[26] A. Osaka, Y. Miura, K. Takeuchi, M. Asada, K. Takahashi, Calcium apatite prepared from calcium hydroxide and orthophosphoric acid, J Mater Sci: Mater Med 2 (1991) 51–55. https://doi.org/10.1007/BF00701687.

[27] B. Basu, J. Vleugels, O.V.D. Biest, Transformation behaviour of tetragonal zirconia: role of dopant content and distribution, Materials Science and Engineering: A 366 (2004) 338–347. https://doi.org/10.1016/j.msea.2003.08.063.

[28] A.C. Ferrari, J. Robertson, Interpretation of Raman spectra of disordered and amorphous carbon, Phys. Rev. B 61 (2000) 14095–14107. https://doi.org/10.1103/PhysRevB.61.14095.

[29] A. Phatak, P. Gupta, S. Mandal, H. Agrawal, O. Parkash, D. Kumar, Hardness-Porosity-Grain Size Interrelationship in Conventionally Sintered 3 mol% Yttria Stabilized Zirconia, High-Temperature Materials 1 (2024) 10008–10008. https://doi.org/10.70322/htm.2024.10008.

[30] H.R. Shafie, M.L. Ballard, Abutment Preparation Techniques for One-Piece Titanium and Zirconia Implants, in: H.R. Shafie (Ed.), Clinical and Laboratory Manual of Dental Implant Abutments, 1st ed., Wiley, 2014: pp. 133–176. https://doi.org/10.1002/9781118928547.ch9.

[31] W. Guo, L. Zhao, P. Li, E. Wang, Y. Pang, Y. Wei, B. Li, Y. Huang, B. Liu, S. Wang, H. You, Y. Long, All-natural ceramic composite bone scaffolds of whitlockite/wollastonite fibers: DLP additive manufacturing, microstructure, and performance, Journal of Materials Research and Technology 33 (2024) 7391–7405. https://doi.org/10.1016/j.jmrt.2024.11.077.

[32] H.A. Badr, A.E. Reda, M.F. Zawrah, R.M. Khattab, H.E.H. Sadek, Effect of Hydroxyapatite on Sinterability, Mechanical Properties, and Bioactivity of Chemically Synthesized Alumina–Zirconia Composites, J. of Materi Eng and Perform 34 (2025) 6125–6137. https://doi.org/10.1007/s11665-024-09531-2.

[33] O. Fakhraei, S. Hesaraki, M. Alizadeh, Evaluation of biphasic calcium phosphate/nanosized 3YSZ composites as toughened materials for bone substitution, Ceramics International 42 (2016) 11201–11208. https://doi.org/10.1016/j.ceramint.2016.04.030.

[34] K. Sakthiabirami, J.-H. Kang, J.-G. Jang, V. Soundharrajan, H.-P. Lim, K.-D. Yun, C. Park, B.-N. Lee, Y.P. Yang, S.-W. Park, Hybrid porous zirconia scaffolds fabricated using additive manufacturing for bone tissue engineering applications, Materials Science and Engineering: C 123 (2021) 111950. https://doi.org/10.1016/j.msec.2021.111950.

[35] S. Komarek, A. Wojteczko, Z. Pędzich, K. Haberko, P. Kwaśniewski, M. Ziąbka, Strength stability over loading time of zirconia-hydroxyapatite composites, Materials Today Communications 37 (2023) 106963. https://doi.org/10.1016/j.mtcomm.2023.106963.

[36] D.-H. Kim, K.-H. Hwang, J.D. Lee, H.-C. Park, S.-Y. Yoon, Long and short range order structural analysis of *In-situ* formed biphasic calcium phosphates, Biomater Res 19 (2015) 14. https://doi.org/10.1186/s40824-015-0036-0.

Supplementary Information

Extrusion-based 3D printing of lightweight bone-mimetic 3YSZ–calcium phosphate composite scaffolds

C.C. Carmo[1], R. Barbosa[1], C. Bianchi[1], M. Brito[1], A. Rovisco[1], A. Baptista[1], J. Marques[2], I. Ferreira[1*].

[1]CENIMAT|i3N, Department of Materials Science, School of Science and Technology, NOVA University Lisbon, Caparica 2829-516, Portugal

[2]Oral Biology and Biochemistry Research Group, Faculdade de Medicina Dentária, UICOB, Universidade de Lisboa, Lisboa, Portugal

*imf@fct.unl.pt

Figure S1 illustrates CAD design of the studied pieces, the printing process and the obtained samples before and after sintering. The dimensions and weight of the samples were measured both prior to and following sintering. The results show a size reduction of approximately 10% to 30% for samples sintered at 1250 ºC and 1450 ºC, respectively.

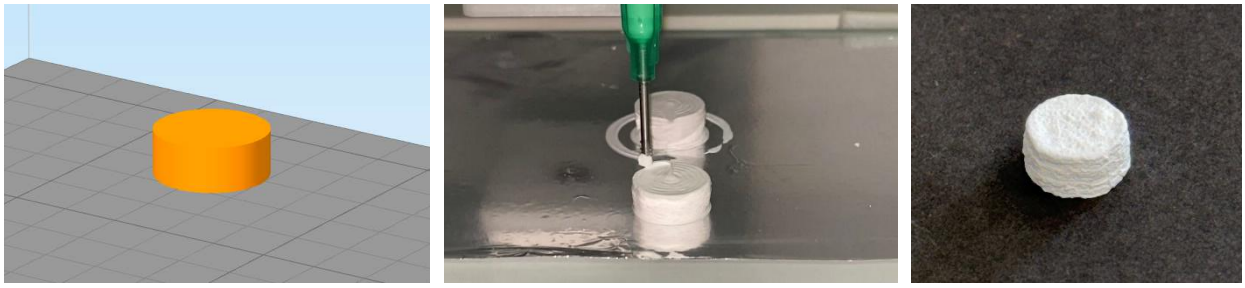


Figure S1 – a) CAD design; b) photo of the printing process; c) photo of samples after sintering.

The SEM surface morphology and EDS analysis was performed and is shown Figure S2. The results indicate a generally uniform distribution of elements and confirm the porous nature of the samples. Minor variations in atomic composition are attributed to differences in the analysed regions. However, an overall composition uniformity is evident, with certain regions being richer in CaP and others in YSZ. This observation also suggests that smoother regions are enriched in CaP, which is clearly illustrated in the images of the 30 wt% CaP and 20 wt% G samples. Overall, the samples show a relatively high carbon content, originating from PVA polymer. During sintering, the polymer burns out, leaving carbon within the samples.

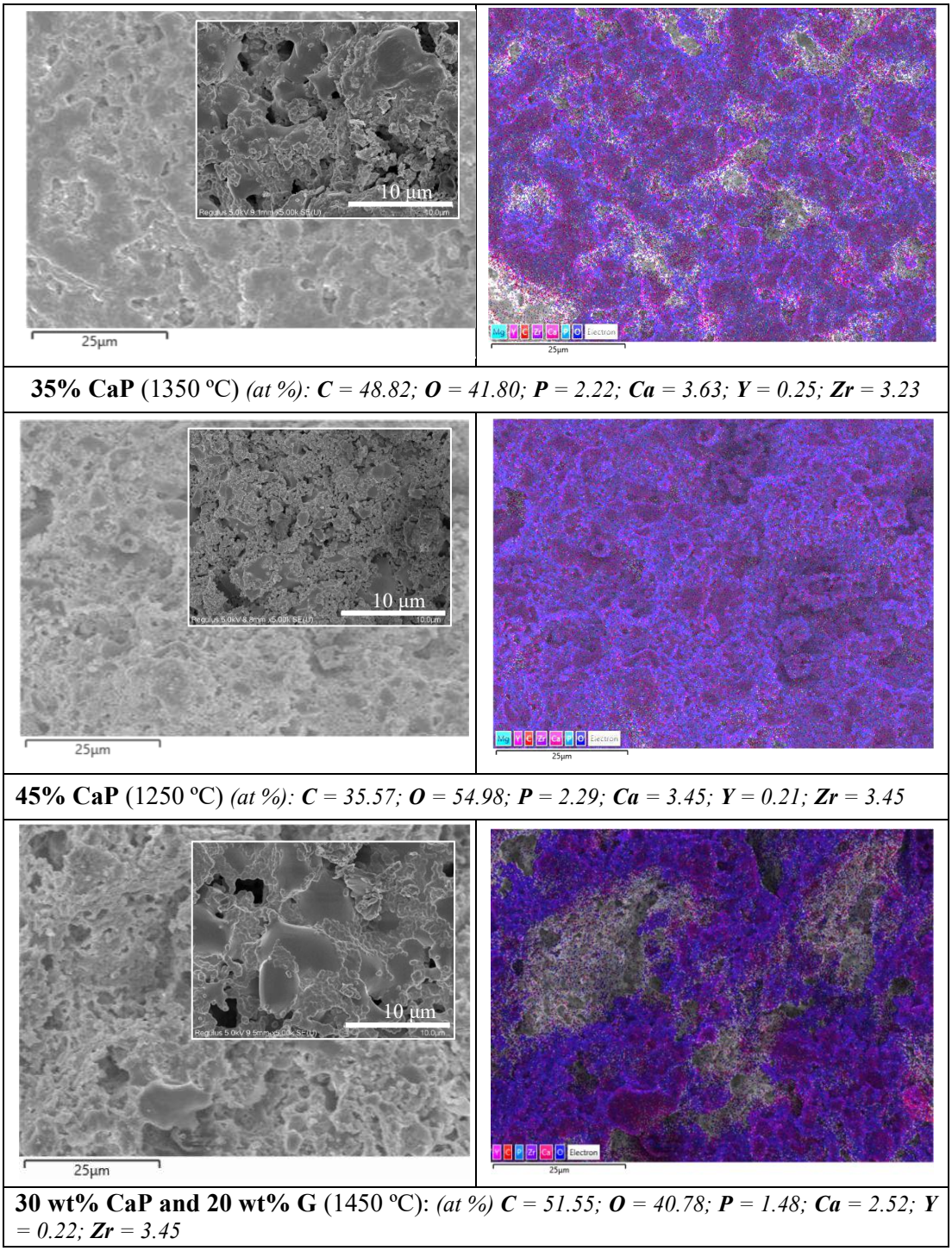


Figure S2 - SEM images and respective EDS mapping and elemental composition expressed in atomic percentage.

The Raman peaks deconvolution is shown in Figure S3. HAp, the most intense feature corresponds to the symmetric stretching (ν_1) P–O mode at 962 cm^{-1}. For β-TCP, the principal vibrations likewise originate from the symmetric stretching (ν_1) P–O mode, appearing as a doublet at 948 and 970 cm^{-1}. The formation of a biphase HAp/β-TCP is possible, leading to a peak deviation, as demonstrated by other authors [36].

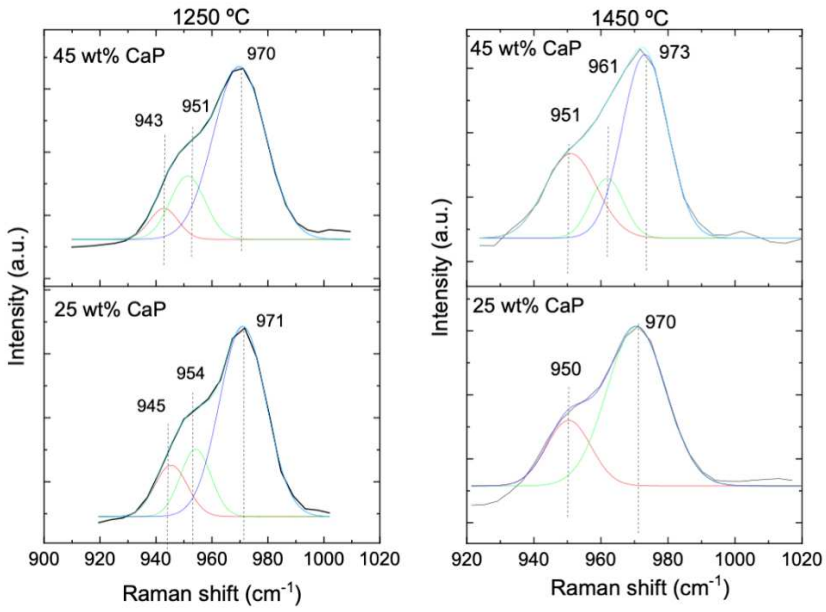
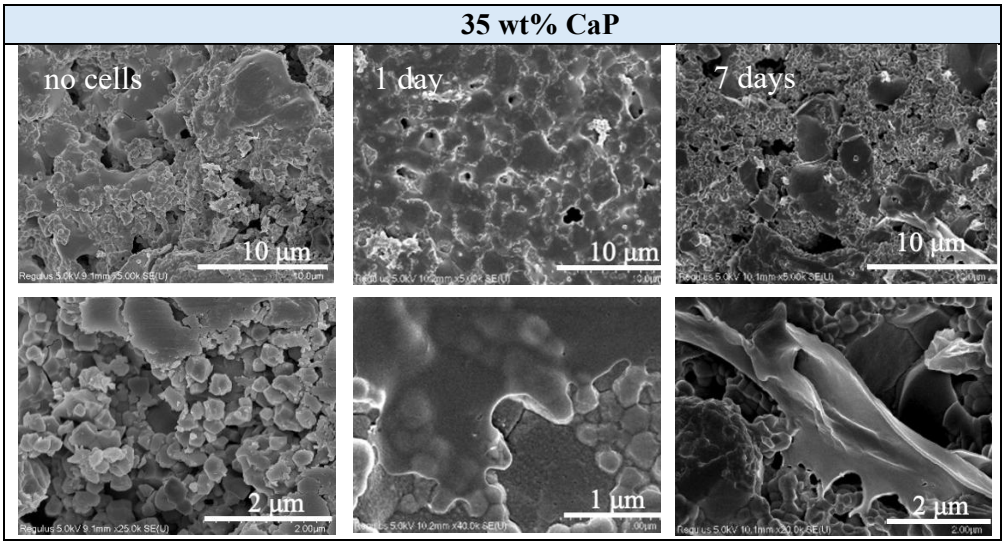


Figure S3 – Deconvolution of Raman peak in the region of PO_4^{3-} vibrational modes for samples sintered at 1250 ºC and 1450ºC.

The progression of HGF-1 cell growth on the composite surfaces is illustrated in Figure S4. SEM images taken at two different magnifications reveal the surface morphology after 1 and 7 days of culture.



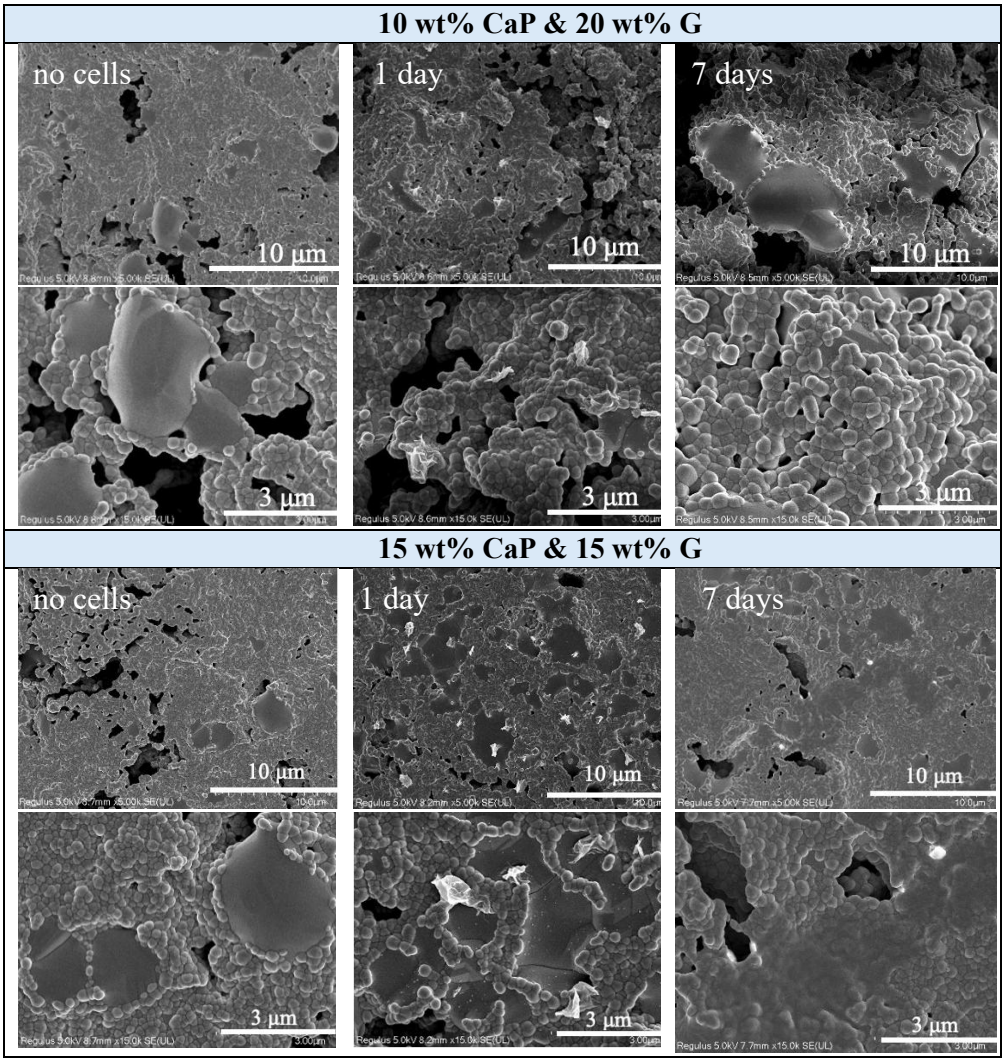


Figure S4 – SEM images of the surfaces: (left) samples without cells, (center) surfaces after 1 day of culture, and (right) surfaces after 7 days of culture.

The extent of cell colonization on the sample surfaces was further evaluated by fluorescence microscopy. Under UV, blue, and green light irradiation, the adherent HGF-1 cells exhibited distinct autofluorescence, with bright green emission under blue light and reddish tones under green light, likely arising from cellular proteins cross-linked during glutaraldehyde fixation. As shown in Figure S5, this imaging approach confirmed successful cell anchoring and surface coverage across all three compositions, providing a qualitative complement to the viability data and SEM observations.

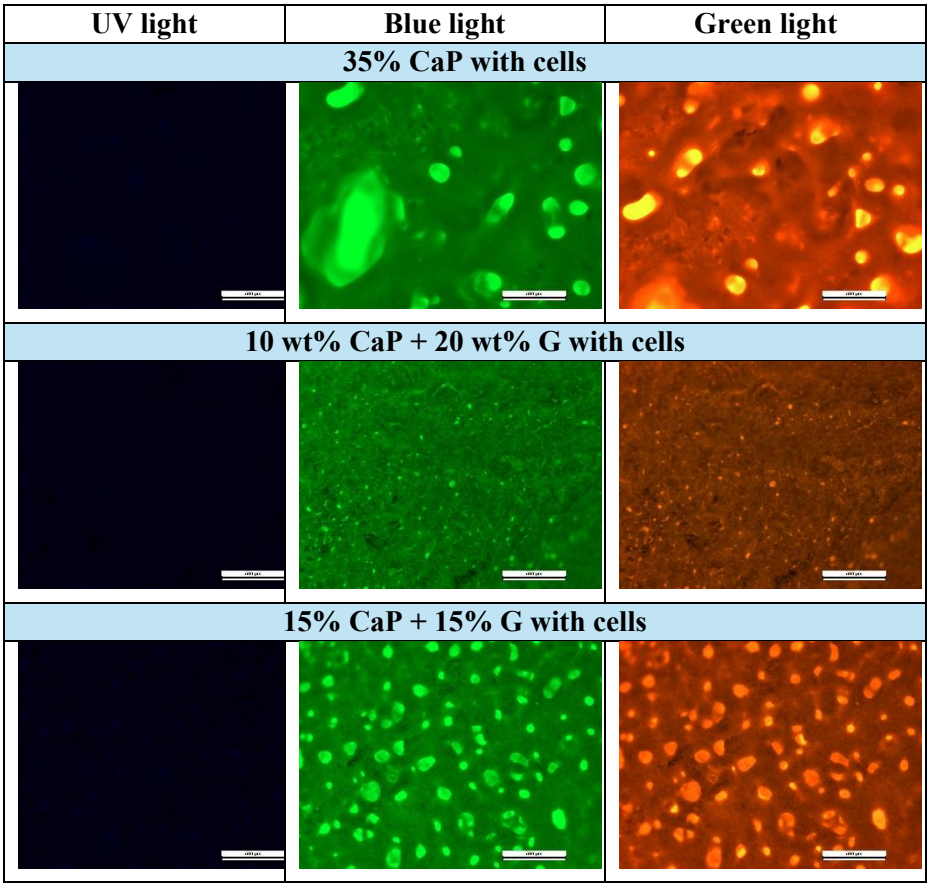


Figure S5 – Microscopy images showing adherent HGF-1 cells fluorescence in samples under UV, blue and green light irradiation. The scale bar represents 500 μm.

References

[1] C.Y. Hu, T.-R. Yoon, Recent updates for biomaterials used in total hip arthroplasty, Biomater Res 22 (2018) 33. https://doi.org/10.1186/s40824-018-0144-8.

[2] M. Ly, S. Spinelli, S. Hays, D. Zhu, 3D Printing of Ceramic Biomaterials, Engineered Regeneration 3 (2022) 41–52. https://doi.org/10.1016/j.engreg.2022.01.006.

[3] R. Galante, C.G. Figueiredo-Pina, A.P. Serro, Additive manufacturing of ceramics for dental applications: A review, Dental Materials 35 (2019) 825–846. https://doi.org/10.1016/j.dental.2019.02.026.

[4] G. Zhong, M. Vaezi, P. Liu, L. Pan, S. Yang, Characterization approach on the extrusion process of bioceramics for the 3D printing of bone tissue engineering scaffolds, Ceramics International 43 (2017) 13860–13868. https://doi.org/10.1016/j.ceramint.2017.07.109.

[5] Y. Wen, S. Xun, M. Haoye, S. Baichuan, C. Peng, L. Xuejian, Z. Kaihong, Y. Xuan, P. Jiang, L. Shibi, 3D printed porous ceramic scaffolds for bone tissue engineering: a review, Biomater. Sci. 5 (2017) 1690–1698. https://doi.org/10.1039/C7BM00315C.

[6] M. Vaezi, H. Seitz, S. Yang, A review on 3D micro-additive manufacturing technologies, Int J Adv Manuf Technol 67 (2013) 1721–1754. https://doi.org/10.1007/s00170-012-4605-2.

[7] J. Brzezińska-Miecznik, K. Haberko, M. Bucko, G. Grabowski, M. Sitarz, Hydroxyapatite of natural origin - zirconia composites, preparation and reactions within the system, PAC 10 (2016) 219–225. https://doi.org/10.2298/PAC1604219B.

[8] Y. Cao, T. Shi, C. Jiao, H. Liang, R. Chen, Z. Tian, A. Zou, Y. Yang, Z. Wei, C. Wang, L. Shen, Fabrication and properties of zirconia/hydroxyapatite composite scaffold based on digital light processing, Ceramics International 46 (2020) 2300–2308. https://doi.org/10.1016/j.ceramint.2019.09.219.

[9] K. Sakthiabirami, J.-H. Kang, J.-G. Jang, V. Soundharrajan, H.-P. Lim, K.-D. Yun, C. Park, B.-N. Lee, Y.P. Yang, S.-W. Park, Hybrid porous zirconia scaffolds fabricated using additive manufacturing for bone tissue engineering applications, Materials Science and Engineering: C 123 (2021) 111950. https://doi.org/10.1016/j.msec.2021.111950.

[10] S. Tarafder, V.K. Balla, N.M. Davies, A. Bandyopadhyay, S. Bose, Microwave-sintered 3D printed tricalcium phosphate scaffolds for bone tissue engineering: 3D Printed TCP Scaffolds for Bone Tissue Engineering, J Tissue Eng Regen Med 7 (2013) 631–641. https://doi.org/10.1002/term.555.

[11] J. Zhang, D. Huang, S. Liu, X. Dong, Y. Li, H. Zhang, Z. Yang, Q. Su, W. Huang, W. Zheng, W. Zhou, Zirconia toughened hydroxyapatite biocomposite formed by a DLP 3D printing process for potential bone tissue engineering, Materials Science and Engineering: C 105 (2019) 110054. https://doi.org/10.1016/j.msec.2019.110054.

[12] H. Fan, L. Wang, R. Dou, Properties of zirconia-doped hydroxyapatite ceramics prepared by vat photopolymerization additive manufacturing technology and microwave sintering, Ceramics International 51 (2025) 25662–25672. https://doi.org/10.1016/j.ceramint.2025.03.248.

[13] H.E. Meema, S. Meema, Compact Bone Mineral Density of the Normal Human Radius, Acta Radiologica: Oncology, Radiation, Physics, Biology 17 (1978) 342–352. https://doi.org/10.3109/02841867809127938.

[14] Poinern, G.E.J.; Brundavanam, R.K.; Fawcett, D., Nanometre scale hydroxyapatite ceramics for bone tissue engineering, (n.d.). https://doi.org/10.5923/j.ajbe.20130306.04.

[15] X. Lu, Y. Zhao, X. Peng, C. Lu, Z. Wu, H. Xu, Y. Qin, Y. Xu, Q. Wang, Y. Hao, D. Geng, Comprehensive Overview of Interface Strategies in Implant Osseointegration, Adv Funct Materials 35 (2025) 2418849. https://doi.org/10.1002/adfm.202418849.

[16] K. Sakthiabirami, J.-H. Kang, J.-G. Jang, V. Soundharrajan, H.-P. Lim, K.-D. Yun, C. Park, B.-N. Lee, Y.P. Yang, S.-W. Park, Hybrid porous zirconia scaffolds fabricated using additive manufacturing for bone tissue engineering applications, Materials Science and Engineering: C 123 (2021) 111950. https://doi.org/10.1016/j.msec.2021.111950.

[17] A. Kumar, P. Kumar, A.S. Dhaliwal, Structural studies of zirconia and yttria doped zirconia for analysing it phase stabilization criteria, IOP Conf. Ser.: Mater. Sci. Eng. 1033 (2021) 012052. https://doi.org/10.1088/1757-899X/1033/1/012052.

[18] D. Xidaki, P. Agrafioti, D. Diomatari, A. Kaminari, E. Tsalavoutas-Psarras, P. Alexiou, V. Psycharis, E. Tsilibary, S. Silvestros, M. Sagnou, Synthesis of Hydroxyapatite, β-Tricalcium Phosphate and Biphasic Calcium Phosphate Particles to Act as Local Delivery Carriers of Curcumin: Loading, Release and In Vitro Studies, Materials 11 (2018) 595. https://doi.org/10.3390/ma11040595.

[19] O. Gorban, I. Danilenko, I. Nosolev, E. Abdullayev, A. Islamov, K. Gavrilenko, A. Doroshkevich, O. Shvets, S. Kolotilov, Impact of chemical and physical modification of zirconia on structure, surface state, and catalytic activity in oxidation of α-tetralol, J Nanopart Res 24 (2022) 197. https://doi.org/10.1007/s11051-022-05566-5.

[20] F. Bakan, A Systematic Study of the Effect of pH on the Initialization of Ca-deficient Hydroxyapatite to β-TCP Nanoparticles, Materials 12 (2019) 354. https://doi.org/10.3390/ma12030354.

[21] V.P. Padmanabhan, R. Kulandaivelu, D. Santhana Panneer, S. Vivekananthan, S. Sagadevan, J. Anita Lett, Microwave synthesis of hydroxyapatite encumbered with ascorbic acid intended for drug leaching studies, Materials Research Innovations 24 (2020) 171–178. https://doi.org/10.1080/14328917.2019.1624940.

[22] S. Ding, J. Zhao, Q. Yu, Effect of Zirconia Polymorph on Vapor-Phase Ketonization of Propionic Acid, Catalysts 9 (2019) 768. https://doi.org/10.3390/catal9090768.

[23] Q. Li, L. Shi, Y. Cai, X. Wang, L. Li, Z. Yuan, W. Tang, Z. Zhan, Effect of graphite on microstructure and friction-wear properties of yttria-stabilized zirconia coatings, Ceramics International 50 (2024) 54116–54124. https://doi.org/10.1016/j.ceramint.2024.10.268.

[24] P.N. Kumar, S. Kannan, Quantitative analysis of the structural stability and degradation ability of hydroxyapatite and zirconia composites synthesized in situ, RSC Adv. 4 (2014) 29946. https://doi.org/10.1039/C4RA02441A.

[25] R. Cuscó, F. Guitián, S. de Aza, L. Artús, Differentiation between hydroxyapatite and β-tricalcium phosphate by means of μ-Raman spectroscopy, Journal of the European Ceramic Society 18 (1998) 1301–1305. https://doi.org/10.1016/S0955-2219(98)00057-0.

[26] A. Osaka, Y. Miura, K. Takeuchi, M. Asada, K. Takahashi, Calcium apatite prepared from calcium hydroxide and orthophosphoric acid, J Mater Sci: Mater Med 2 (1991) 51–55. https://doi.org/10.1007/BF00701687.

[27] B. Basu, J. Vleugels, O.V.D. Biest, Transformation behaviour of tetragonal zirconia: role of dopant content and distribution, Materials Science and Engineering: A 366 (2004) 338–347. https://doi.org/10.1016/j.msea.2003.08.063.

[28] A.C. Ferrari, J. Robertson, Interpretation of Raman spectra of disordered and amorphous carbon, Phys. Rev. B 61 (2000) 14095–14107. https://doi.org/10.1103/PhysRevB.61.14095.

[29] A. Phatak, P. Gupta, S. Mandal, H. Agrawal, O. Parkash, D. Kumar, Hardness-Porosity-Grain Size Interrelationship in Conventionally Sintered 3 mol% Yttria Stabilized Zirconia, High-Temperature Materials 1 (2024) 10008–10008. https://doi.org/10.70322/htm.2024.10008.

[30] H.R. Shafie, M.L. Ballard, Abutment Preparation Techniques for One-Piece Titanium and Zirconia Implants, in: H.R. Shafie (Ed.), Clinical and Laboratory Manual of Dental Implant Abutments, 1st ed., Wiley, 2014: pp. 133–176. https://doi.org/10.1002/9781118928547.ch9.

[31] W. Guo, L. Zhao, P. Li, E. Wang, Y. Pang, Y. Wei, B. Li, Y. Huang, B. Liu, S. Wang, H. You, Y. Long, All-natural ceramic composite bone scaffolds of whitlockite/wollastonite fibers: DLP additive manufacturing,

microstructure, and performance, Journal of Materials Research and Technology 33 (2024) 7391–7405. https://doi.org/10.1016/j.jmrt.2024.11.077.

[32] H.A. Badr, A.E. Reda, M.F. Zawrah, R.M. Khattab, H.E.H. Sadek, Effect of Hydroxyapatite on Sinterability, Mechanical Properties, and Bioactivity of Chemically Synthesized Alumina–Zirconia Composites, J. of Materi Eng and Perform 34 (2025) 6125–6137. https://doi.org/10.1007/s11665-024-09531-2.

[33] O. Fakhraei, S. Hesaraki, M. Alizadeh, Evaluation of biphasic calcium phosphate/nanosized 3YSZ composites as toughened materials for bone substitution, Ceramics International 42 (2016) 11201–11208. https://doi.org/10.1016/j.ceramint.2016.04.030.

[34] K. Sakthiabirami, J.-H. Kang, J.-G. Jang, V. Soundharrajan, H.-P. Lim, K.-D. Yun, C. Park, B.-N. Lee, Y.P. Yang, S.-W. Park, Hybrid porous zirconia scaffolds fabricated using additive manufacturing for bone tissue engineering applications, Materials Science and Engineering: C 123 (2021) 111950. https://doi.org/10.1016/j.msec.2021.111950.

[35] S. Komarek, A. Wojteczko, Z. Pędzich, K. Haberko, P. Kwaśniewski, M. Ziąbka, Strength stability over loading time of zirconia-hydroxyapatite composites, Materials Today Communications 37 (2023) 106963. https://doi.org/10.1016/j.mtcomm.2023.106963.

[36] D.-H. Kim, K.-H. Hwang, J.D. Lee, H.-C. Park, S.-Y. Yoon, Long and short range order structural analysis of *In-situ* formed biphasic calcium phosphates, Biomater Res 19 (2015) 14. https://doi.org/10.1186/s40824-015-0036-0.